



OPEN

An artificial intelligence method using FDG PET to predict treatment outcome in diffuse large B cell lymphoma patients

Maria C. Ferrández^{1,2}✉, Sandeep S. V. Golla^{1,2}, Jakoba J. Eertink^{2,3}, Bart M. de Vries^{1,2}, Pieternella J. Lugtenburg⁴, Sanne E. Wiegers^{1,2}, Gerben J. C. Zwezerijnen^{1,2}, Simone Piepenbosch^{2,3}, Lars Kurch⁵, Andreas Hüttmann⁶, Christine Hanoun⁶, Ulrich Dührsen⁶, Henrica C. W. de Vet^{7,8}, PETRA*^{*}, Josée M. Zijlstra^{2,3} & Ronald Boellaard^{1,2}

Convolutional neural networks (CNNs) may improve response prediction in diffuse large B-cell lymphoma (DLBCL). The aim of this study was to investigate the feasibility of a CNN using maximum intensity projection (MIP) images from ¹⁸F-fluorodeoxyglucose (¹⁸F-FDG) positron emission tomography (PET) baseline scans to predict the probability of time-to-progression (TTP) within 2 years and compare it with the International Prognostic Index (IPI), i.e. a clinically used score. 296 DLBCL ¹⁸F-FDG PET/CT baseline scans collected from a prospective clinical trial (HOVON-84) were analysed. Cross-validation was performed using coronal and sagittal MIPs. An external dataset (340 DLBCL patients) was used to validate the model. Association between the probabilities, metabolic tumour volume and Dmax_{bulk} was assessed. Probabilities for PET scans with synthetically removed tumours were also assessed. The CNN provided a 2-year TTP prediction with an area under the curve (AUC) of 0.74, outperforming the IPI-based model (AUC = 0.68). Furthermore, high probabilities (>0.6) of the original MIPs were considerably decreased after removing the tumours (<0.4, generally). These findings suggest that MIP-based CNNs are able to predict treatment outcome in DLBCL.

Diffuse large B-cell lymphoma (DLBCL) is an aggressive lymphoid malignancy which originates in the B lymphocytes and accounts for 30% of the total annual diagnoses of Non-Hodgkin lymphoma in western countries¹. A widely used first-line therapy in DLBCL combines rituximab, cyclophosphamide, doxorubicin, vincristine, and prednisone (R-CHOP). The number of R-CHOP cycles and/or initial usage of more intense chemotherapy regimens initially depends on the primary disease stage and the International Prognostic Index (IPI), which defines a patient's risk profile². IPI score includes age, World Health Organization performance status, Ann Arbor stage, serum lactate dehydrogenase level, and number of extranodal sites of disease. ¹⁸F-fluorodeoxyglucose (¹⁸F-FDG) positron emission tomography (PET)—computed tomography (CT) imaging allows highly accurate visualization of DLBCL tumours, which is therefore the essential modality for appropriate staging. Moreover, ¹⁸F-FDG PET is frequently used as an early outcome prediction marker, since complete metabolic response early throughout (i.e. interim) therapy allows de-escalation of treatment cycles³. This interim-PET adaptive treatment approach is increasingly integrated into national recommendations on DLBCL. Despite better identification of low-risk patients at baseline and early during treatment, overall, one-third of DLBCL patients do not respond

¹Cancer Center Amsterdam, Department of Radiology and Nuclear Medicine, Amsterdam UMC, Vrije Universiteit Amsterdam, Amsterdam UMC, Amsterdam, The Netherlands. ²Cancer Center Amsterdam, Imaging and Biomarkers, Amsterdam, The Netherlands. ³Cancer Center Amsterdam, Department of Hematology, Amsterdam UMC, Vrije Universiteit Amsterdam, Amsterdam, The Netherlands. ⁴Department of Hematology, Erasmus MC Cancer Institute, University Medical Center Rotterdam, Rotterdam, The Netherlands. ⁵Department of Nuclear Medicine, Clinic and Polyclinic for Nuclear Medicine, University of Leipzig, Leipzig, Germany. ⁶Department of Hematology, West German Cancer Center, University Hospital Essen, University of Duisburg-Essen, Essen, Germany. ⁷Department of Epidemiology and Data Science, Amsterdam Public Health Research Institute, Amsterdam UMC, Vrije Universiteit Amsterdam, Amsterdam, The Netherlands. ⁸Department of Methodology, Amsterdam Public Health Research Institute, Methodology, Amsterdam, The Netherlands. *A list of authors and their affiliations appears at the end of the paper. ✉email: m.c.ferrandezferrandez@amsterdamumc.nl

to first-line treatment or relapse¹. Therefore, early identification of high-risk patients is important as patients might benefit from a more tailored treatment strategy.

Quantitative parameters extracted from ¹⁸F-FDG PET/CT scans provide insight into the tumour characteristics. From these parameters, metabolic tumour volume (MTV) has been repeatedly reported as a promising prognostic factor in DLBCL^{4–6}. The inclusion of dissemination features like the maximal distance between the largest lesion and any other lesion ($D_{\max, \text{bulk}}$), in combination with MTV, has further improved risk stratification of patients⁵. To obtain these parameters, tumour segmentation requires user interaction for each ¹⁸F-FDG PET/CT scan which can be time consuming and depends on the observers interpretation. The implementation of artificial intelligence (AI) and convolutional neural networks (CNNs) might be able to reduce and/or replace these tasks. CNNs can extract high-level features from multi-dimensional input data (i.e. images). In oncology, CNNs are already being investigated to automate different medical image classification tasks: diagnostics⁷, tumour delineation and segmentation^{8–10}, extraction of PET features surrogates¹¹ and disease progression and/or treatment outcome prediction^{12,13}. Two of the main drawbacks of CNNs are the computational expense they entail and the high complexity of its extracted features, especially when it comes to 3D image analysis such as with PET/CT scans. Alternatively, maximum intensity projections (MIPs) of ¹⁸F-FDG PET/CT scans can be used as 2D inputs for the CNN, decreasing data dimension and complexity and, thereby, decreasing the computational load and cost^{14,15}.

The aim of this study was to investigate the feasibility of a CNN for the prediction of 2-year time-to-progression (TTP) in DLBCL patients using MIP images derived from ¹⁸F-FDG PET/CT baseline scans. The models outcome is a binary prediction given by the probability of TTP longer than 2 years $P(\text{TTP0})$ or TTP shorter than 2 years $P(\text{TTP1})$, where TTP1 indicates an increased risk of tumour progression for the patient. TTP0 may indicate absence of tumour progression or absence of recurrence.

Materials and methods

Datasets. In this study we used two different datasets of baseline DLBCL ¹⁸F-FDG PET/CT scans: the HOVON-84 dataset¹⁶ was used to train the CNN model whereas the PETAL dataset¹⁷ was used as an external validation of the models performance. All patients from both datasets provided written consent for the use of their data. After correction for IPI, there were no significant differences in survival between the PETAL and HOVON-84 study¹⁸. Both studies were approved by institutional review boards and all included patients provided informed consent. The use of all data within the PETRA imaging database has been approved by the institutional review board of the VU University Medical Center (JR/20140414).

HOVON-84. Three hundred seventy-three DLBCL patients who underwent baseline ¹⁸F-FDG PET/CT from the multicenter HOVON-84 trial (EudraCT, 2006-005,174-42) were included in this study. The main inclusion/exclusion criteria from this trial can be found elsewhere¹⁶. From these, 317 diagnosed DLBCL patients were included in this analysis. Missing essential DICOM (Digital Imaging and Communication in Medicine) information and incomplete whole-body scans were the main reason for exclusion. Furthermore, 7 patients were lost to follow-up within 2 years and 14 other patients died within 2 years of unrelated reasons. This led to a total of 296 DLBCL patients included in the study. Of which, 244 were classified as TTP0 and 52 as TTP1. In this paper, we used the exact same data as previously published by Eertink et al.⁴ to allow for direct comparison of our results.

PETAL. The external validation was performed using diagnosed DLBCL patients from the multicenter PETAL trial (EudraCT 2006-001641-33) who underwent baseline ¹⁸F-FDG PET/CT. The eligibility for the PETAL trial is described elsewhere¹⁷. Initially, the trial consisted of 1098 PETAL patients. Reasons to exclude patients were as follows: diagnosis other than DLBCL, incomplete scans or with artefacts or missing DICOM information. This led to a total of 395 DLBCL patients with associated ¹⁸F-FDG PET/CT baselines scans available for this study. Moreover, 12 underwent a different treatment to R-CHOP, 24 patients were lost for follow-up within 2 years, and 19 died without progression. This led to a total of 340 patients. From these, 279 were classified as TTP0 and 61 as TTP1. The exact same data were used as in Eertink et al.^{4,19}, so that our results can be compared with recently published segmentation based approaches.

Quality control of scans. The participating sites provided the scans in DICOM format. The scans were subsequently anonymised. For QC we used criteria described by EANM guidelines: mean standardized uptake value (SUVmean) of the liver should be between 1.3 and 3.0 and the plasma glucose level lower than 11 mmol/L³. The QC criteria are described in detail elsewhere⁴.

Maximum intensity projections. The ACCURATE tool was used to obtain the so-called lesion masks which are the images that contain only the lymphoma tumour(s) segmentation²⁰. The segmentation of the tumours was performed using a SUV threshold of 4.0. This was found to be the preferred segmentation threshold, as shown by Barrington et al.²¹. Any physiological uptake adjacent to tumours was manually deleted. The conversion to MIP images was performed using a preprocessing tool developed in Interactive Data Language (IDL®, NV5 Geospatial Solutions, Inc). This tool generates coronal and sagittal MIPs with size $275 \times 200 \times 1$ and a pixel size of 4×4 mm. MIPs were generated for lesion MIPs (MIPs containing only tumours) and for the complete PET scans. Examples of these coronal and sagittal MIPs can be found in Fig. 1. The MIPs were normalized by a fixed maximum intensity value ($\text{SUV} = 40$). This was selected based on the maximum tumour intensity value found across the scans. The values above this maximum were truncated to avoid normalization to be driven by the SUV value of high uptake organs such as the bladder.

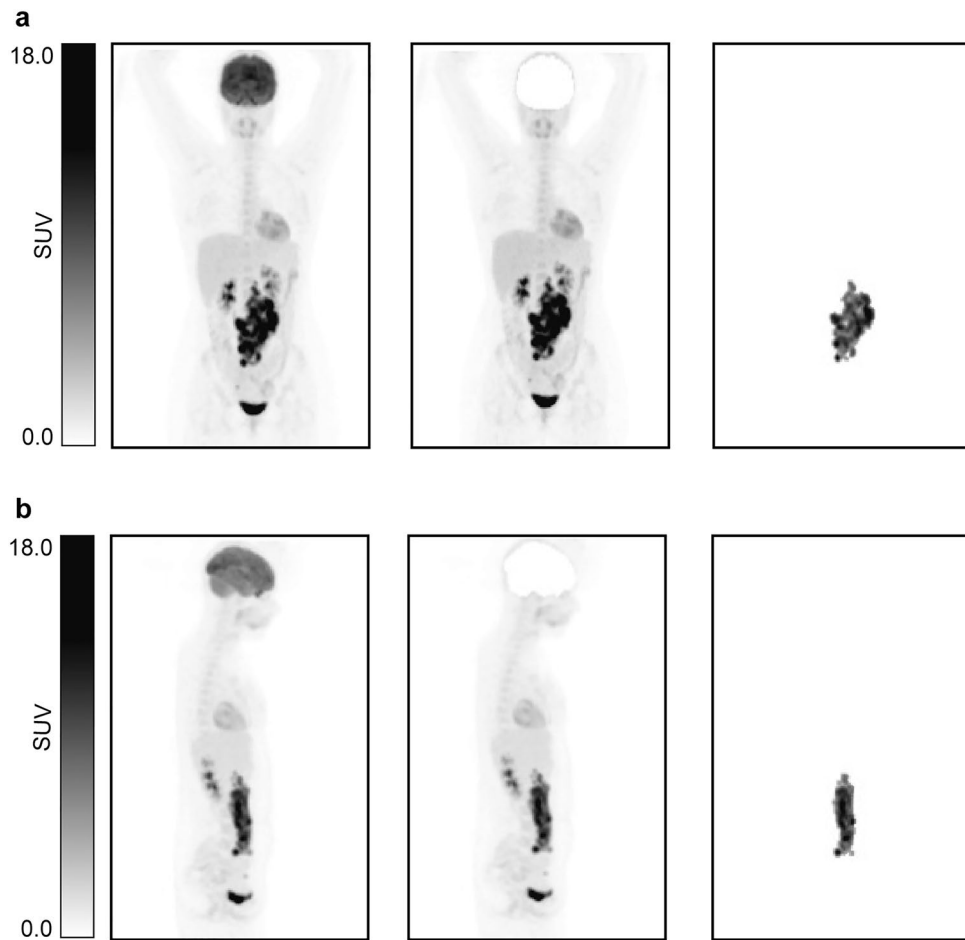


Figure 1. Illustration of the different MIPs implemented in this study. **(a)** Coronal view. **(b)** Sagittal view. From left to right: MIP, MIP without brain and lesion MIP.

Data sampling scheme. Since the training dataset classes were highly unbalanced (244 TTP0 vs 52 TTP1), we applied a data sampling scheme where the TTP0s were divided into 5 equally stratified data subsets: 4 subsets of 49 patients (subsets A-D) and 1 subset of 48 patients (subset E). Additionally, 3 randomly selected TTP0 patients belonging to different subsets, were added to each of these subsets in order to achieve a total of 52 TTP0s per subset (subset E with 51 TTP0s), which matched the total number of TTP1s. Eventually, each subset contained a total of 104 patients with a prevalence of 50% for each class (subset E with 103 patients). The details of this scheme can be found in Fig. 2. Each subset (A to E) was trained using a fivefold cross validation (for each cross validation run, the data was split into two sets: training set (80%) and internal validation set (20%)).

Convolutional neural network. The CNN consists of two branches, one receives the coronal MIP as input and the other one receives the sagittal MIP as input, which are merged as a last step to yield the final prediction. Coronal and sagittal MIPs are analysed independently but in parallel by an identical multi-layer architecture. The CNN design consists of 4 convolution layers, each one of these are followed by a max pooling layer. In a CNN, the convolution layer uses different filters over the image to extract low level features (e.g. edges, gradients) in earlier layers and high level features in deeper layers. In our CNN, the feature maps are doubled at each convolution layer, starting at 16 in the first layer and going up to 128 in the last layer, and their dimensions continuously decrease by (3,3). In each convolution layer the rectified linear unit (ReLU) activation function is applied. After each convolution layer, a dropout of 0.35 is applied, indicating that 35% of the network nodes and connections are randomly dropped from the CNN in order to prevent overfitting. Right after the dropout, a MaxPooling layer was implemented. The MaxPooling layer acts as the dimensionality reduction layer. There are 3 Maxpooling layers in our CNN, each of these with feature map sizes of (3,3), (3,3) and (2,2). After the last convolution and SpatialDropout layer, the CNN is connected to a GlobalAveragePooling2D (GAP2D) layer also known as ‘flattening’ layer. This layer ‘flattens’ the output from the convolution layers into a less complex shape (i.e. a 2D tensor). The coronal and sagittal outputs are then concatenated at the final dense layer or fully connected layer (FCL) which generates an output for two different classes: TTP0 and TTP1. A softmax function is introduced to generate a probability for each of these classes, which is the final CNN output the probability of TTP longer than 2 years, $P(\text{TTP0})$, and the probability of TTP shorter than 2 years, $P(\text{TTP1})$ both add up to 1.

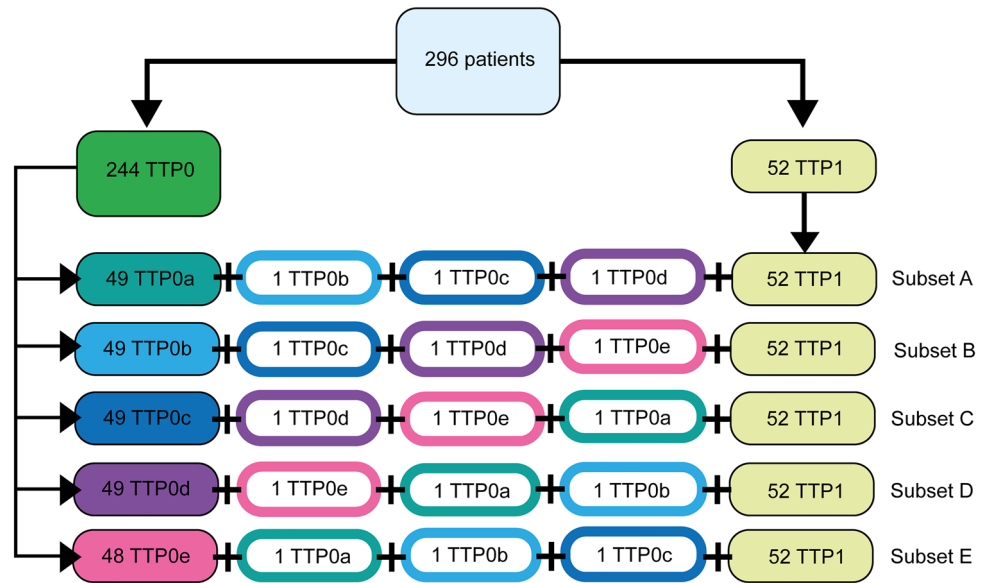


Figure 2. Data sampling scheme. Diagram representation of the five data subsets, with four subsets (A–D) consisting of 52 stratified TTP0 subjects and all 52 TTP1 subjects. One of the five subsets (subset E) contained 51 stratified TTP0 and all 52 TTP1 subjects.

The classifier was compiled using the Adam optimizer with a learning rate (LRt) of 0.00005 and a decay rate (DR) of 0.000001. The CNN structure is illustrated in Fig. 3.

In this study we trained the model following 3 different training schemes. These are illustrated in Supplemental Figure 1: training based on (1) only-lesion MIPs (Lesion MIP CNN); (2) lesion MIPs and regular MIPs (MIP CNN); (3) lesion MIPs and MIPs after removal of the brain, brain removed MIPs (BR-MIP CNN). The network architecture is kept the same. This approach was followed in order to explore if the model could be trained to recognize pathological patterns.

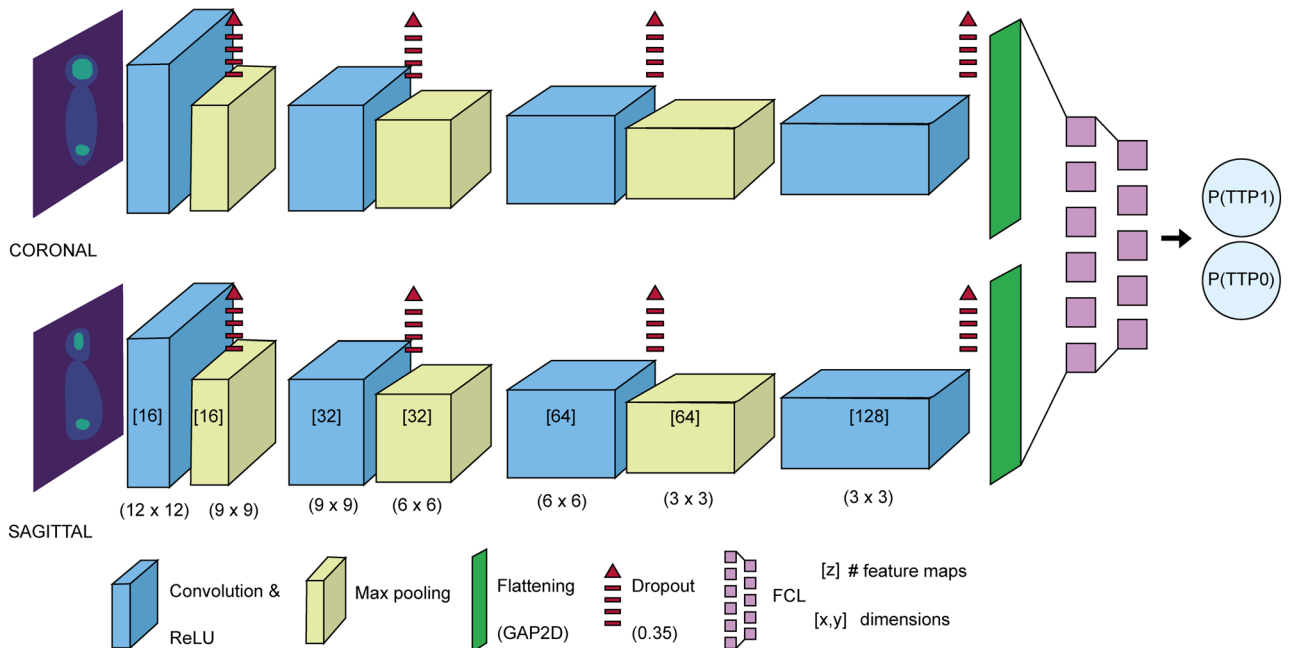


Figure 3. CNN architecture. In the convolution layers, the number of feature maps is shown, followed by the size of these matrices. The max pooling layers are depicted with the feature detector dimensions. A spatial dropout and the ReLU activation function were applied to each convolution layer. The model was compiled using the Adam optimizer, with LRt=0.00005 and DR=0.000001. Coronal and sagittal outputs are concatenated in the dense layer or fully connected layer (FCL).

CNN	CV-AUC (SD)		Sensitivity (SD)		Specificity (SD)	
	Training	Validation	Training	Validation	Training	Validation
Lesion MIP	0.81 (0.02)	0.75 (0.07)	0.69 (0.06)	0.63 (0.19)	0.76 (0.02)	0.73 (0.08)
MIP	0.79 (0.03)	0.70 (0.06)	0.76 (0.04)	0.75 (0.08)	0.64 (0.06)	0.55 (0.10)
BR-MIP	0.77 (0.09)	0.72 (0.11)	0.73 (0.17)	0.71 (0.14)	0.69 (0.11)	0.63 (0.19)

Table 1. Cross-validation (\pm SD) of AUC, sensitivity, and specificity for training and internal validation (HOVON-84 dataset) for the model associated with subset C. AUC area under the curve, SD standard deviation.

The lesion MIP CNN uses only the lesion MIPs as input (Fig. 1). These MIPs contain only the information and intensity of the tumours. The lesions MIPs of both coronal and sagittal views were used to train and validate the model for 200 epochs.

The MIP CNN uses both lesion MIPs and MIPs for the training of the model. The lesion masks contain only information of the tumours but not the intensity values. The training of the MIP CNN consisted in two subsequent steps. Firstly, the lesions masks of both coronal and sagittal MIPs were used to train and validate the model for 200 epochs. In the second step, the pre-trained model on the lesion masks was re-trained and re-validated for another 300 epochs, this time using the regular coronal and sagittal MIP images instead. The same patients were used for training of the two steps.

The BR-MIP CNN follows the same training process as the MIP CNN but instead of the original MIPs, it uses MIPs without brain (Fig. 1). MIP brain removal was performed in order to provide greater consistency across the dataset since not all scans included the head. The process of removing the brains is described in detail in Supplemental Material 1²².

In the case of the MIP CNN and the BR-MIP CNN, the classifier required only the MIP images to make the predictions. The idea behind these two CNNs was to generate a classifier where the prediction is free of the observer-dependent tumour segmentation.

All models were implemented using Python version 3.9.16, Keras version 2.10.0 and Tensorflow library version 2.10.0.

Plausibility of the CNN. To better understand the CNN predictions, we further investigated the output of the model by exploring the association between P(TTP1) and two PET extracted features: MTV and $D_{max_{bulk}}$ since both have shown potential as prognostic markers in DLBCL^{4,5,19,23}. The process to extract PET features has been explained in previous studies⁴. Moreover, we synthetically removed the tumours from the MIP images to simulate tumour-free data and evaluated the CNN predictions on this data. The tumours were masked using the lesion MIPs generated using the in-house built preprocessing tool. The voxel values corresponding to the tumours were replaced by an average of the voxel intensities excluding the background. This process is shown in Supplemental Figure 2.

To facilitate representation, the TTP1 probabilities obtained through the CNN were calibrated by performing a logistic regression fit with the probabilities as input and the TTP0/TTP1 labels as outcome²⁴. The obtained regression fit coefficients were then applied to the CNN TTP1 probabilities generated after removing the tumours in order to accordingly calibrate the tumour-free MIPs CNN TTP1 probabilities.

Statistical analysis. The receiver operating characteristic (ROC) and the area under the curve (AUC) were used to evaluate the CNN performance. During training, the fold with the highest cross validated (CV-)AUC across the 5 folds was preserved. See Supplemental Material 2 for more details²⁵. The PETAL dataset was used to externally validate the CNN model. This performance evaluation process was performed for the lesion MIP CNN, MIP CNN and BR-MIP CNN. The cut-off value to determine sensitivity and specificity for every model was set to 0.5. AUCs were statistically compared using the Delong test to assess the performance of different CNN models to that of an IPI-based prediction model²⁶. This IPI model defines patients with risk factor of 4 or higher as high-risk patients (i.e. TTP1)⁴. The association of the TTP1 probabilities and the PET-extracted features (MTV and $D_{max_{bulk}}$) was assessed using Pearson's correlation coefficient.

Ethical approval. All individual participants included in the study gave written informed consent to participate in the study. The HOVON-84 study was approved by the institutional review board of the Erasmus MC (2007-055) and was performed in accordance with the ethical standards as laid down in the 1964 Declaration of Helsinki and its later amendments or comparable ethical standards. The PETAL study was approved by the Federal Institute for Drugs and Medical Devices and the ethics committees of all participating sites (University Hospital Essen and Deutsche Krebshilfe; ClinicalTrials.gov NCT00554164).

Results

A summary of the characteristics of the datasets can be found in Supplemental Table 1.

Internal validation. The results for the fivefold CV for the 5 data subsets (A–E) can be found in the Supplemental Tables 2–4. The average performance of the models (associated with each subset) can be found in

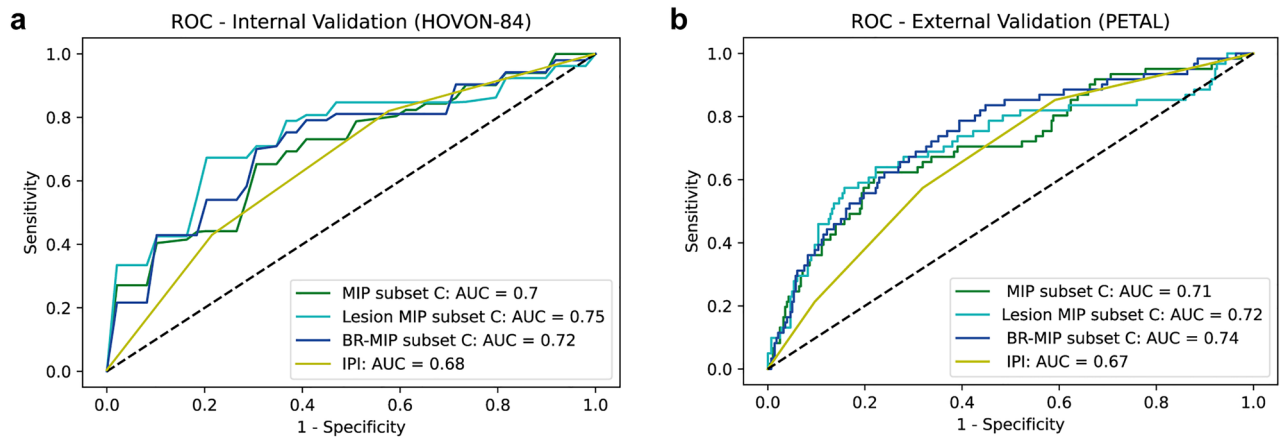


Figure 4. Receiver Operator Curves. (a) ROC and AUC for internal validation performed on HOVON-84 dataset for the model trained on subset C (following fivefold cross validation). (b) ROC and AUC for external validation performed on PETAL dataset using the model trained on subset C. For reference, a model without any predictive performance is depicted (AUC=0.5).

CNN	AUC	Sensitivity	Specificity
Lesion MIP	0.72	0.59	0.8
MIP	0.71	0.62	0.72
BR-MIP	0.74	0.54	0.81

Table 2. AUC, sensitivity and specificity for external validation data (PETAL dataset) for the model associated with subset C. AUC area under the curve.

Supplemental Figure 3a. The model trained with subset C was best performing in all cases (Supplemental Figure 4). The AUCs for the model trained on subset C for Lesion MIP CNN, MIP CNN and BR-MIP CNN are illustrated in Fig. 4a and the CV-AUCs are given in Table 1. These values are comparable or better to the ones obtained from the IPI prediction model (AUC was reported as 0.68 for the HOVON-84 dataset)⁴. Delong test showed statistical significant differences between the AUC curves for the BR-MIP CNN and the IPI prediction model (p value = 0.015).

External validation. The PETAL dataset was used to externally validate the performance of the CNNs. The average performance of the models (associated with each subset) can be found in Supplemental Figure 3b. The model trained with subset C was again the best performing trained model (Supplemental Figure 5). The ROC plot with the corresponding AUC values for each CNN are shown in Fig. 4b. A summary of the performance of the 3 CNNs is given in Table 2. The BR-MIP CNN outperformed the IPI model with an AUC of 0.67, sensitivity = 0.57 and specificity = 0.68 (Delong test, p -value = 0.035). We provided some examples of the BR-MIP CNN predictions in Supplemental Figure 6.

Plausibility of the CNN. The BR-MIP CNN (trained using subset C) was used to further investigate the feasibility of the model for TTP prediction. A moderate association for MTV with P(TTP1) and a weak association for $D_{\text{max}_{\text{bulk}}}$ with P(TTP1) was found for HOVON-84 (Fig. 5a, b) and a moderate association for both MTV and $D_{\text{max}_{\text{bulk}}}$ with P(TTP1) was found for PETAL (Fig. 5c, d). In all scenarios, higher P(TTP1) seemed to be related to higher MTV and $D_{\text{max}_{\text{bulk}}}$ values. These features have been previously reported as promising prognostic factors in DLBCL⁴⁻⁶.

After generating new probabilities for the tumour-free MIPs in the PETAL dataset, we found that these were generally lower when compared to the initial probabilities obtained from the images with tumours. This is the case, specially, for probabilities over 0.6, which, after tumour removal, were decreased to values below 0.4. Some examples are given in Supplemental Figure 7 for different patients with decreased probabilities after tumour removal. The histogram of P(TTP1)s is shown in Fig. 6 for both datasets: original MIPs (with tumours) and tumour-free MIPs.

Discussion

In this study, we investigated the feasibility of a CNN model for the prediction of progression after 2 years in DLBCL patients using ¹⁸F-FDG PET/CT MIP images. Our model was internally (HOVON-84 dataset) and externally validated (PETAL dataset) to assess the performance of the model in a different dataset¹⁸. Proper external validation is one of the main limitations seen across AI studies^{27,28}. Poor or insufficient validation causes

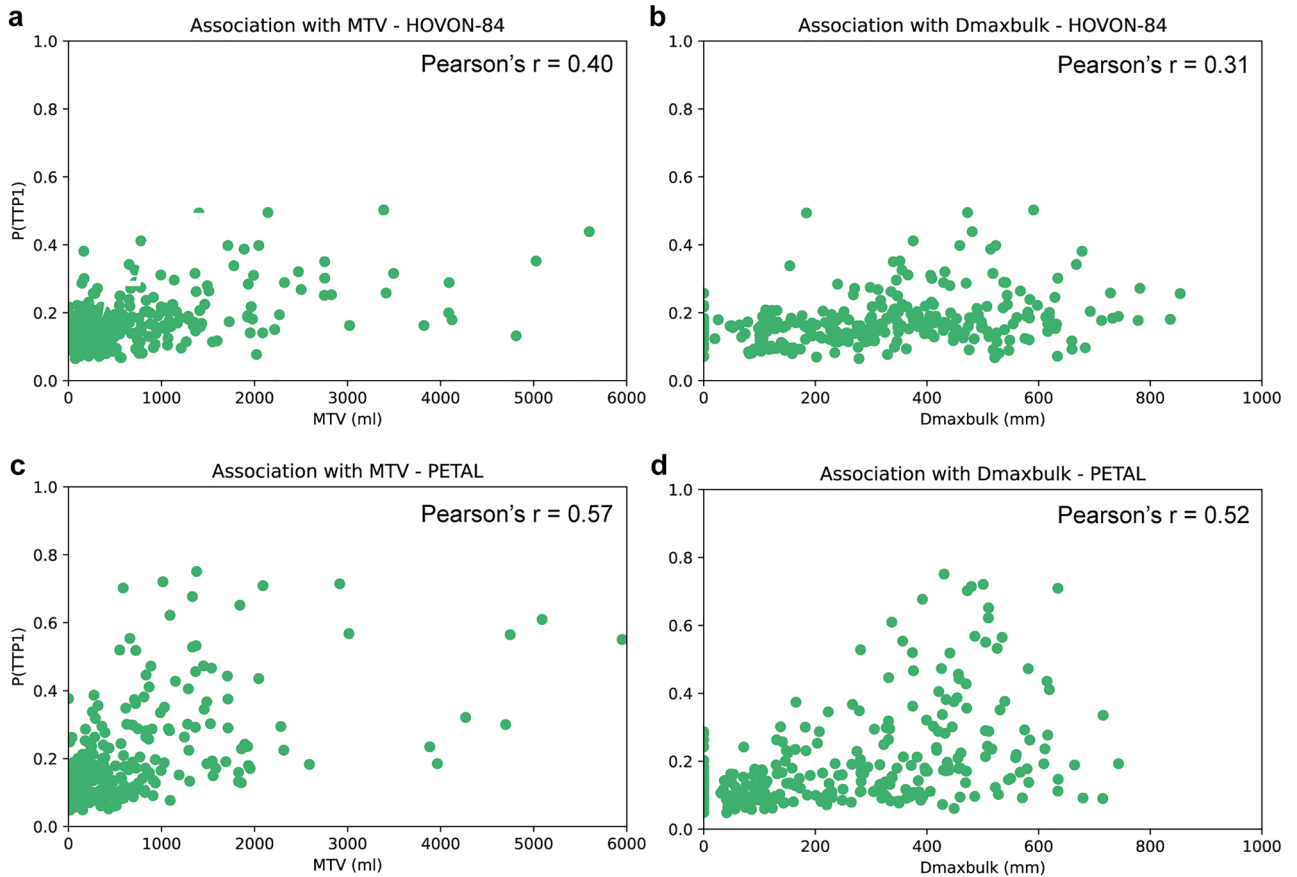


Figure 5. Association between TTP1 probabilities and PET features: (a, b) HOVON84 TTP1 probabilities for MTV and $D_{max_{bulk}}$ respectively. (c, d) PETAL TTP1 probabilities for MTV and $D_{max_{bulk}}$ respectively.

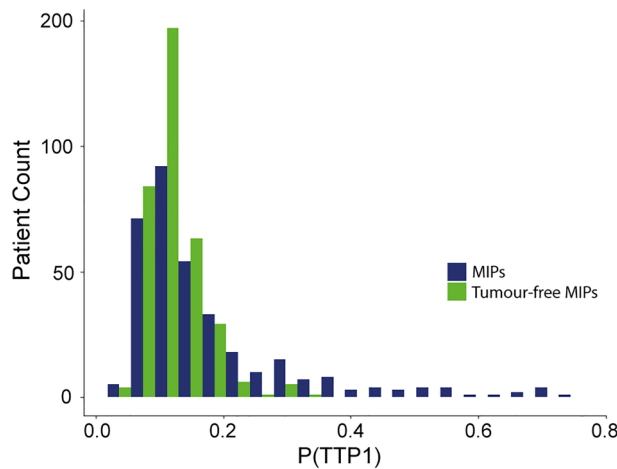


Figure 6. Histogram for the PETAL TTP1 probabilities. Probabilities for MIPs shown in dark blue and probabilities after removing the tumours (i.e. tumour-free MIPs) shown in green.

misleading results and limits translation into the clinical setting²⁹. In our external validation, the CNN showed an improved predictive performance compared to the IPI model (AUC of 0.74 vs 0.67, Delong test p-value = 0.035). In a recent paper by Westin et al.³⁰, it is recommended to assess progression within or after 1-year of the first line treatment. We decided to use 2-year TTP because at the time of this study, it remained clinically relevant^{31–34} but most importantly, to be able to compare our model performance with results seen in previous studies^{4,19}.

Features extracted from PET scans are currently being investigated to predict outcome of DLBCL patients with promising results^{4,19,23,33,35}. Mikhaeel et al.²³ recently published the International Metabolic Prognostic

Index which included Ann Arbor stage, age and MTV for the prediction of 3-year progression free survival (PFS). Moreover, Eertink et al.⁴ developed a model that combined PET-extracted features (including MTV and $D_{max_{bulk}}$) with clinical parameters, yielding a CV-AUC of 0.77 for the prediction of 2-year TTP in an internal validation using scans from the HOVON-84 trial.

In addition, there is an increasing interest in the use of CNNs as segmentation tools. Several studies have shown the potential of CNNs for lesion segmentation in lymphoma patients with outstanding results when comparing surrogate PET features to PET features extracted from manually segmented lesions^{9,36–38}. These models are easy to understand, especially in a clinical setting. The segmentation of the lesions can be easily inspected visually and allows direct inspection of tumour volume, dissemination and any other extracted feature, that are used for prediction. The potential of segmentation-based CNNs is unquestionable and for this reason we intent to investigate their role in DLBCL treatment outcome prediction in the future and compare these with deep learning based end-to-end methods.

In this study, we aimed to assess the feasibility of a deep learning model that does not rely on segmentation and generates predictions directly from the PET images. It is important to highlight the fact that this study is meant to be a first step in the exploratory analysis of using end-to-end CNNs. However, these models are difficult to use due to their complexity and lack of interpretability³⁹. In addition to these challenges, it is not yet known whether end-to-end CNNs could outperform segmentation-based models and/or radiomic models and therefore, the use of segmentation based AI approaches in combination with handcrafted radiomics analysis should also be further explored.

Currently, there are only a few studies which have looked at the applications of end-to-end CNNs. Liu et al.⁴⁰ developed a multi task 3D U-Net for both tumour segmentation and prediction of PFS in DLBCL with outstanding results when compared to radiomic-based models and single task CNNs. Moreover, the use of MIPs for treatment outcome prediction in DLBCL is currently being investigated^{15,40,41}. Rebaud et al.⁴¹ trained a multi-task ranker neural network using coronal MIP images which performed as well as TMTV for DLBCL PFS prediction. However, these studies did not assess the performance of the model in external datasets as indicated in the RELAINCE guidelines²⁹. To our best knowledge, this is the first paper to investigate the feasibility of CNNs for ‘deep’ treatment outcome prediction in DLBCL patients using ¹⁸F-FDG PET/CT MIP images and to investigate its performance in an external dataset.

We trained the CNN in 3 different ways: lesion MIP, MIP and BR-MIP CNN. The BR-MIP CNN was kept for the CNN plausibility analysis as it outperformed the IPI-based model and predicted 2-year TTP with the highest AUC in the external dataset. Moreover, compared to the lesion MIP, BR-MIP CNN does not require prior tumour segmentation to make predictions and, compared to the MIP CNN, BR-MIP model uses MIP images without brain uptake. The main reason to remove the brain is that it brings consistency across the dataset as, in some PET studies, the head was not (fully) included during acquisition.

In order to better understand the output of our model, we investigated whether there was any relation between the CNN outcome probabilities with MTV and $D_{max_{bulk}}$, since both of them have prognostic capabilities for DLBCL. Even though a weak association was found for $D_{max_{bulk}}$ with HOVON-84 predictions, our results suggests that the CNN is capturing information that might be related to tumour volume and dissemination but also that other image characteristics influence the CNN prediction. Deep learning methods tend to pay more attention to textural features⁴². In this context, conventional PET parameters, although easier to understand, might be missing relevant information for tumour progression. Another technique we used to examine the plausibility of the model is ‘ablating’ the tumours from the MIPs. The decrease in P(TTP1) values suggest that the CNN is indeed mainly using tumour information to make the predictions. Furthermore, when looking at a few examples of the CNN output (Supplemental Figure 6) we found that patients with fewer tumours and lower dissemination are given lower probability values than patients with more tumours and higher dissemination. Even though further analysis is needed, these findings suggest that the model associates tumour dissemination with a higher risk of disease progression.

Regarding the limitations of this study, DLBCL patients can develop lesions near or within the brain which might complicate brain removal. Even after addressing this issue, there were around 1% of patients with truncated lesions which could not be solved. It is therefore important to consider clinician supervision in these cases. Another limitation of this study is the cut-off value used to calculate the sensitivity and specificity, based on the HOVON-84 dataset, which led to certain differences in the PETAL dataset. Slight adjustment of this value might be required to achieve comparable results in terms of sensitivity and specificity in external datasets. Moreover, HOVON-84 trial did not include patients with Ann Arbor stage 1 disease and patients who had central nervous system involvement were also excluded from the trials. The lack of limited stage and DLBCL patients with very poor prognosis could be a potential bias for the model performance and its generalizability. A more extensive external validation is required to assess the generalizability of the model.

As mentioned earlier, end-to-end CNNs are complex and interpretation of results is difficult. In this study we partially addressed this by looking at associations with known PET parameters and analysing tumour intensities contribution. However, these issues make the translation into the clinic challenging. Nevertheless, we believe more research in this field is required to unravel the potential of end-to-end CNNs.

Conclusion

In this study we introduced a CNN model capable of predicting 2-year TTP in DLBCL patients using ¹⁸F-FDG PET/CT MIP images as input. The CNN model predicted 2-year TTP in DLBCL patients better than IPI scores. Moreover, it was illustrated that the model prediction is affected by the presence or absence of lesions. Even though further investigations are necessary, our current findings suggest that CNNs using MIPs have potential as outcome prediction models.

Code availability

The code and the model weights will be available as a supplementary zip file upon publication of the manuscript.

Received: 31 March 2023; Accepted: 7 August 2023

Published online: 12 August 2023

References

- Crump, M. *et al.* Outcomes in refractory diffuse large B-cell lymphoma: Results from the international scholar-1 study. *Blood* **130**, 1800–1808 (2017).
- Galaznik, A. *et al.* Predicting outcomes in patients with diffuse large B-cell lymphoma treated with standard of care. *Cancer Inform.* **18**, 1176935119835538 (2019).
- Boellaard, R. *et al.* FDG PET/CT: EANM procedure guidelines for tumour imaging: Version 2.0. *Eur. J. Nucl. Med. Mol. Imaging* **42**, 328–354 (2015).
- Eertink, J. J. *et al.* (18)F-FDG PET baseline radiomics features improve the prediction of treatment outcome in diffuse large B-cell lymphoma. *Eur. J. Nucl. Med. Mol. Imaging* **49**, 932–942 (2022).
- Cottreau, A. S. *et al.* (18)F-FDG PET dissemination features in diffuse large B-cell lymphoma are predictive of outcome. *J. Nucl. Med.* **61**, 40–45 (2020).
- Schmitz, C. *et al.* Dynamic risk assessment based on positron emission tomography scanning in diffuse large B-cell lymphoma: Post-hoc analysis from the petal trial. *Eur. J. Cancer* **124**, 25–36 (2020).
- Bi, L. *et al.* Automatic detection and classification of regions of FDG uptake in whole-body PET-CT lymphoma studies. *Comput. Med. Imaging Graph.* **60**, 3–10 (2017).
- Sibille, L. *et al.* (18)F-FDG PET/CT uptake classification in lymphoma and lung cancer by using deep convolutional neural networks. *Radiology* **294**, 445–452 (2020).
- Blanc-Durand, P. *et al.* Fully automatic segmentation of diffuse large B cell lymphoma lesions on 3D FDG PET/CT for total metabolic tumour volume prediction using a convolutional neural network. *Eur. J. Nucl. Med. Mol. Imaging* **48**, 1362–1370 (2021).
- Chen, L. *et al.* Automatic pet cervical tumor segmentation by combining deep learning and anatomic prior. *Phys. Med. Biol.* **64**, 085019 (2019).
- Girum, K. B. *et al.* (18)F-FDG PET maximum intensity projections and artificial intelligence: A win-win combination to easily measure prognostic biomarkers in dlbc patients. *J. Nucl. Med.* (2022).
- Fujima, N. *et al.* Deep learning analysis using FDG-PET to predict treatment outcome in patients with oral cavity squamous cell carcinoma. *Eur. Radiol.* **30**, 6322–6330 (2020).
- Guo, R. *et al.* Weakly supervised deep learning for determining the prognostic value of (18)F-FDG PET/CT in extranodal natural killer/t cell lymphoma, nasal type. *Eur. J. Nucl. Med. Mol. Imaging* **48**, 3151–3161 (2021).
- Takehiko Fujiwara, M. M., Watanuki, S., Mejia, M. A. & Itoh, M. Hiroshi Fukuda Easy detection of tumor in oncologic whole-body PET by projection reconstruction images with maximum intensity projection algorithm. *Ann. Nucl. Med.* **13**, 199–203 (1999).
- Boellaard, R. *et al.* Artificial Intelligence based outcome classification from baseline 18F-FDG PET/CT in de novo diffuse large B-cell lymphoma patients. European association of nuclear medicine October 20–23, 2021 virtual. *Eur. J. Nucl. Med. Mol. Imaging* **48**, 348 (2021).
- Lugtenburg, P. J. *et al.* Rituximab-chop with early rituximab intensification for diffuse large B-cell lymphoma: A randomized phase III trial of the HOVON and the NORDIC lymphoma group (HOVON-84). *J. Clin. Oncol.* **38**, 3377–3387 (2020).
- Duhrsen, U. *et al.* Positron emission tomography-guided therapy of aggressive non-hodgkin lymphomas (PETAL): A multicenter, randomized phase III trial. *J. Clin. Oncol.* **36**, 2024–2034 (2018).
- Eertink, J. J. *et al.* Optimal timing and criteria of interim pet in DLBCL: A comparative study of 1692 patients. *Blood Adv.* **5**, 2375–2384 (2021).
- Eertink, J. J. *et al.* Baseline pet radiomics outperforms the IPI risk score for prediction of outcome in diffuse large B-cell lymphoma. *Blood* **141**, 3055–3064 (2023).
- Boellaard, R. Quantitative oncology molecular analysis suite: Accurate. *J. Nucl. Med.* **59**, 1753 (2018).
- Barrington, S. F. *et al.* Automated segmentation of baseline metabolic total tumor burden in diffuse large B-cell lymphoma: Which method is most successful? A study on behalf of the PETRA consortium. *J. Nucl. Med.* **62**, 332–337 (2021).
- Otsu, N. A threshold selection method from gray-level histograms. *IEEE Trans. Syst. Man Cybern.* **9**, 62–66 (1979).
- Mikhaeel, N. G. *et al.* Proposed new dynamic prognostic index for diffuse large B-cell lymphoma: International metabolic prognostic index. *J. Clin. Oncol.* **40**, 2352–2360 (2022).
- Eertink, J. J. *et al.* External validation: A simulation study to compare cross-validation versus holdout or external testing to assess the performance of clinical prediction models using pet data from DLBCL patients. *EJNMMI Res.* **12**, 58 (2022).
- Levy, P. S. Clinical epidemiology: The essentials. *JAMA* **250**, 1469–1469 (1983).
- DeLong, E. R., DeLong, D. M., & Clarke-Pearson, D. L. Comparing the areas under two or more correlated receiver operating characteristic curves: A nonparametric approach. *Biometrics*, 837–845 (1988).
- Corti, C. *et al.* Artificial intelligence for prediction of treatment outcomes in breast cancer: Systematic review of design, reporting standards, and bias. *Cancer Treat. Rev.* **108**, 102410 (2022).
- Frood, R. *et al.* Baseline PET/CT imaging parameters for prediction of treatment outcome in hodgkin and diffuse large B cell lymphoma: A systematic review. *Eur. J. Nucl. Med. Mol. Imaging* **48**, 3198–3220 (2021).
- Jha, A. K. *et al.* Nuclear medicine and artificial intelligence: Best practices for evaluation (the RELIANCE guidelines). *J. Nucl. Med.* **63**, 1288–1299 (2022).
- Westin, J. & Sehn, L. H. CAR T cells as a second-line therapy for large B-cell lymphoma: A paradigm shift?. *Blood* **139**, 2737–2746 (2022).
- Aide, N., Fruchart, C., Nganoa, C., Gac, A. C. & Lasnon, C. Baseline (18)F-FDG PET radiomic features as predictors of 2-year event-free survival in diffuse large B cell lymphomas treated with immunochemotherapy. *Eur. Radiol.* **30**, 4623–4632 (2020).
- Zhang, R., Cheng, C., Zhao, X. & Li, X. Multiscale mask R-CNN-based lung tumor detection using PET imaging. *Mol. Imaging* **18**, 1536012119863531 (2019).
- Kostakoglu, L. *et al.* A prognostic model integrating PET-derived metrics and image texture analyses with clinical risk factors from GOYA. *EJHaem* **3**, 406–414 (2022).
- Mikhaeel, N. G. *et al.* FDG PET/CT after two cycles of R-CHOP in DLBCL predicts complete remission but has limited value in identifying patients with poor outcome: Final result of a UK national cancer research institute prospective study. *Br. J. Haematol.* **192**, 504–513 (2021).
- Cottreau, A. S. *et al.* Risk stratification in diffuse large B-cell lymphoma using lesion dissemination and metabolic tumor burden calculated from baseline PET/CT(dagger). *Ann. Oncol.* **32**, 404–411 (2021).
- Jemaa, S. *et al.* Full automation of total metabolic tumor volume from FDG PET/CT in dlbc for baseline risk assessments. *Cancer Imaging* **22**, 39 (2022).

37. Weisman, A. J. *et al.* Convolutional neural networks for automated PET/CT detection of diseased lymph node burden in patients with lymphoma. *Radiol. Artif. Intell.* **2**, e200016 (2020).
38. Weisman, A. J. *et al.* Automated quantification of baseline imaging pet metrics on FDG PET/CT images of pediatric hodgkin lymphoma patients. *EJNMMI Phys.* **7**, 76 (2020).
39. Shortliffe, E. H. & Sepulveda, M. J. Clinical decision support in the era of artificial intelligence. *JAMA* **320**, 2199–2200 (2018).
40. Liu, P., Zhang, M., Gao, X., Li, B. & Zheng, G. Joint lymphoma lesion segmentation and prognosis prediction from baseline FDG PET images via multitask convolutional neural networks. *IEEE Access* **10**, 81612–81623 (2022).
41. Rebaud, L. *et al.* Multitask learning-to-rank neural network for predicting survival of diffuse large b-cell lymphoma patients from their unsegmented baseline [18F]FDG PET/CT scans. *J. Nucl. Med.* **63**, 3250–3250 (2022).
42. Kubilius, J., Bracci, S. & Op de Beek, H. P. Deep neural networks as a computational model for human shape sensitivity. *PLoS Comput. Biol.* **12**, e1004896 (2016).

Acknowledgements

This work was financially supported by the Hanarth Fonds Fund and the Dutch Cancer Society (#VU-2018-11648). The sponsor had no role in gathering, analyzing or interpreting the data. The authors thank all the patients who participated in the trials and all of the member of the PETRA consortium which names and affiliations are given in the Supplementary Material. Figures 2 and 3 were designed and drawn by M.C.F. The rest of the figures were generated with Python (version 3.9).

Author contributions

S.S.V.G. and R.B. contributed to the concept and design of the study. P.J.L. and U.D. were responsible for acquiring and collecting the data. C.H., S.P., J.J.E., S.E.W. and M.C.F. performed the data analysis. M.C.F. performed the training of the model, validation of the results and completed the first draft of the manuscript. P.J.L., U.D., L.K., A.H., C.H., S.P., S.E.W., B.M.d.V., J.J.E., S.S.V.G., R.B., G.J.C.Z., H.C.W.V. and J.M.Z. reviewed and approved the manuscript.

Competing interests

This work was financially supported by the Hanarth Fonds Fund and the Dutch Cancer Society (#VU-2018-11648). M.C.F., S.S.V.G., J.J.E., B.M.d.V., S.E.W., G.J.C.Z., S.P., L.K., A.H., C.H., U.D., H.C.W.d.V. and R.B. declare no competing financial interests. P.J.L. received research funding from Takeda, Servier and Roche and received honoraria for advisory boards from Takeda, Servier, Genentech, Genmab, Celgene, Incyte and AbbVie. J.M.Z. received research funding from Roche and received honoraria for advisory boards from Takeda, Gilead, BMS and Roche. No other potential conflicts of interest relevant to this article exist.

Additional information

Supplementary Information The online version contains supplementary material available at <https://doi.org/10.1038/s41598-023-40218-1>.

Correspondence and requests for materials should be addressed to M.C.F.

Reprints and permissions information is available at www.nature.com/reprints.

Publisher's note Springer Nature remains neutral with regard to jurisdictional claims in published maps and institutional affiliations.



Open Access This article is licensed under a Creative Commons Attribution 4.0 International License, which permits use, sharing, adaptation, distribution and reproduction in any medium or format, as long as you give appropriate credit to the original author(s) and the source, provide a link to the Creative Commons licence, and indicate if changes were made. The images or other third party material in this article are included in the article's Creative Commons licence, unless indicated otherwise in a credit line to the material. If material is not included in the article's Creative Commons licence and your intended use is not permitted by statutory regulation or exceeds the permitted use, you will need to obtain permission directly from the copyright holder. To view a copy of this licence, visit <http://creativecommons.org/licenses/by/4.0/>.

© The Author(s) 2023

PETRA

Josée M. Zijlstra^{2,3}, Ronald Boellaard^{1,2}, Henrica C. W. de Vet^{7,8}, Otto S. Hoekstra^{2,3},
 Jakoba J. Eertink^{2,3}, Coreline N. Burggraaff³, Sanne E. Wieggers^{4,2}, Simone Pieplensbosch^{2,3},
 Maria C. Ferrández^{1,2}, Sandeep S. V. Golla^{1,2}, Gerben J. C. Zwezerijnen^{1,2},
 Annelies Bes³, Martijn W. Heymans^{7,8}, Yvonne W. S. Jauw^{2,3}, Pieternella J. Lugtenburg⁴,
 Martine E. D. Chamuleau³, Sally F. Barrington⁹, George Mikhaeel¹⁰, Lars Kurch⁵,
 Andreas Hüttmann⁶, Christine Hanoun⁶, Ulrich Dührsen⁶, Emanuele Zucca^{11,12},
 Luca Ceriani^{11,13}, Robert Carr¹⁴, Tamás Györke^{15,16}, Sándor Czibor¹⁷, Stefano Fanti^{18,19,20},
 Lale Kostakoglu²¹, Annika Loft²², Martin Hutchings²³ & Sze Ting Lee²⁴

⁹King's College London and Guy's and St Thomas' PET Centre, School of Biomedical Engineering and Imaging Sciences, King's Health Partners, King's College London, London, UK. ¹⁰Department of Clinical Oncology, Guy's

Cancer Centre and School of Cancer and Pharmaceutical Sciences, King's College London University, London, UK. ¹¹SAKK Swiss Group for Clinical Cancer Research, Bern, Switzerland. ¹²Department of Oncology, IOSI - Oncology Institute of Southern Switzerland, Università Della Svizzera Italiana, Bellinzona, Switzerland. ¹³Department of Nuclear Medicine and PET/CT Centre, Imaging Institute of Southern Switzerland, Università Della Svizzera Italiana, Bellinzona, Switzerland. ¹⁴Guy's and St. Thomas' Hospital, King's College, London, UK. ¹⁵Department of Nuclear Medicine, Semmelweis University, Budapest, Hungary. ¹⁶ScanoMed Medical Diagnostic Research and Training Ltd., Budapest, Hungary. ¹⁷Medical Imaging Centre, Department of Nuclear Medicine, Semmelweis University, Budapest, Hungary. ¹⁸Nuclear Medicine Unit, IRCCS Azienda Ospedaliero-Universitaria di Bologna, Bologna, Italy. ¹⁹Radiology Unit, IRCCS Azienda Ospedaliero-Universitaria di Bologna, Bologna, Italy. ²⁰Nuclear Medicine, Alma Mater Studiorum, University of Bologna, Bologna, Italy. ²¹Department of Radiology and Medical Imaging, University of Virginia, Charlottesville, VA, USA. ²²Department of Clinical Physiology and Nuclear Medicine, Rigshospitalet, Copenhagen, Denmark. ²³Department of Haematology, Rigshospitalet, Copenhagen, Denmark. ²⁴Australasian Association of Nuclear Medicine Specialists, Balmain, NSW, Australia.